Received: 11 March 2022 | Revised: 13 June 2022 | Accepted: 15 June 2022

DOI: 10.1002/ar.25027

FULL LENGTH ARTICLE

The Anatomical Record | WILEY

Contrast-enhanced micro-computed tomography of compartment and time-dependent changes in femoral cartilage and subchondral plate in a murine model of osteoarthritis

Deva D. Chan[1,2,3] | **Maleeha Mashiatulla**[4] | **Jun Li**[1] | **Ryan D. Ross**[4] | **Meghana Pendyala**[3] | **Amit Patwa**[5,6,7] | **Mark W. Grinstaff**[5,6] | **Anna Plaas**[1] | **D. Rick Sumner**[4]

[1]Department of Internal Medicine, Rush University Medical Center, Chicago, Illinois, USA

[2]Weldon School of Biomedical Engineering, Purdue University, West Lafayette, Indiana, USA

[3]Department of Biomedical Engineering, Center for Biotechnology and Interdisciplinary Studies, Rensselaer Polytechnic Institute, Troy, New York, USA

[4]Department of Anatomy and Cell Biology, Rush University Medical Center, Chicago, Illinois, USA

[5]Department of Biomedical Engineering Department of Chemistry, Boston University, Boston, Massachusetts, USA

[6]Department of Chemistry, Boston University, Boston, Massachusetts, USA

[7]Division of Chemistry, Navrachana University, Vadodara, Gujarat, India

Correspondence
Deva D. Chan, Purdue University,
206 S. Martin Jischke Drive, MJIS 3023,
West Lafayette, IN 47907, USA.
Email: chand@purdue.edu

Abstract

A lack of understanding of the mechanisms underlying osteoarthritis (OA) progression limits the development of effective long-term treatments. Quantitatively tracking spatiotemporal patterns of cartilage and bone degeneration is critical for assessment of more appropriately targeted OA therapies. In this study, we use contrast-enhanced micro-computed tomography (μCT) to establish a timeline of subchondral plate (SCP) and cartilage changes in the murine femur after destabilization of the medial meniscus (DMM). We performed DMM or sham surgery in 10–12-week-old male C57Bl/6J mice. Femora were imaged using μCT after 0, 2, 4, or 8 weeks. Cartilage-optimized scans were performed after immersion in contrast agent CA4+. Bone mineral density distribution (BMDD), cartilage attenuation, SCP, and cartilage thickness and volume were measured, including lateral and medial femoral condyle and patellar groove compartments. As early as 2 weeks post-DMM, cartilage thickness significantly increased and cartilage attenuation, SCP volume, and BMDD mean significantly decreased. Trends in cartilage and SCP metrics within each

Deva D. Chan and Maleeha Mashiatulla shared first authorship.

joint compartment reflected those seen in global measurements, and both BMDD and SCP thickness were consistently greater in the lateral and medial condyles than the patellar groove. Sham surgery also resulted in significant changes to SCP and cartilage metrics, highlighting a potential limitation of using surgical models to study tissue morphology or composition changes during OA progression. Contrast-enhanced μCT analysis is an effective tool to monitor changes in morphology and composition of cartilage, and when combined with bone-optimized μCT, can be used to assess the progression of degenerative changes after joint injury.

KEYWORDS

cartilage, contrast-enhanced micro-computed tomography, murine model, post-traumatic osteoarthritis, subchondral plate

1 | INTRODUCTION

Osteoarthritis (OA) is a highly prevalent disease with limited treatment options (Murphy & Helmick, 2012). Currently available treatments include surgical corrections and intraarticular injections to decrease the inflammatory response, but no interventions halt or reverse damage to tissue structure and biomechanical function. Development of an effective disease-modifying OA drug is partly hindered by an incomplete understanding of the mechanisms of OA onset and progression (Vincent, 2020). Although some genetic predispositions are associated with increased risk of OA development (Miyamoto et al., 2007; Valdes & Spector, 2008), for many patients, precise mechanisms and timing of onset and progression are often uncertain.

OA studies typically focus on cartilage and bone due to the severity of structural, biochemical, and mechanical changes in these tissues. Several studies describe the mechanism of onset in both tissues, and the crosstalk between subchondral bone and cartilage is well established in in vitro and in vivo models (Goldring, 2012; Lin et al., 2010; Lories & Luyten, 2011; Pan et al., 2012; Sanchez et al., 2005; Westacott et al., 1997). However, even in well-defined animal models of OA, it often remains unclear whether degenerative changes develop and progress first in the bone or the cartilage (Alliston et al., 2018; Goldring & Goldring, 2016). Alternatively, cartilage and subchondral bone may respond simultaneously, particularly in cases of joint instability and post-traumatic OA. Because the progression of OA may differ depending on the initiation, it is important to measure with high spatial resolution the structural and compositional changes that both bone and cartilage undergo to further understanding of OA progression and to guide the development and assessment of appropriately timed and targeted therapies.

A critical barrier to understanding the progression of OA changes in bone and cartilage, especially within commonly used murine model studies, is the lack of quantitative tools capable of sensitively analyzing structural and compositional changes in both tissues, within the same specimen and at micron-level resolutions. While micro-computed tomography (μCT) has long been used to assess three-dimensional (3D) bone morphology and mineral density (Bouxsein et al., 2010), measurements of cartilage structure and composition are often limited to 2D histology and semi-quantitative scoring systems (Glasson et al., 2010; Pritzker et al., 2006). To overcome this limitation, we utilize nondestructive, high-resolution μCT with an iodinated, cationic contrast agent that partitions preferentially to the negatively charged proteoglycans in cartilage (Bansal, Joshi, et al., 2011; Bansal, Stewart, et al., 2011; Mashiatulla, Moran, et al., 2017; Stewart et al., 2013) but can target any negatively charged tissues present. High-resolution measurements of structure and composition in both cartilage and subchondral bone are thus possible with a single imaging modality and within the same sample. In addition, x-ray attenuation in cartilage with cationic contrast agents correlates to glycosaminoglycan (GAG) content and mechanical properties (Lakin et al., 2016). Thus, μCT provides 3D tissue morphology alongside measurements of extracellular matrix composition within cartilage and subchondral bone, making it a powerful tool to assess animal models of OA.

In this study, contrast-enhanced μCT using CA4+ (Mashiatulla, Moran, et al., 2017) enables a timeline of femoral bone and cartilage changes in mice after surgical destabilization of the medial meniscus (DMM) (Glasson et al., 2007). We constructed this profile of OA progression using mice euthanized at 0, 1, 2, 4, and 8 weeks after DMM. Subchondral plate (SCP) thickness, volume, and bone mineral density distribution (BMDD) were quantified from high-resolution μCT images. Cartilage thickness, volume, and mean x-ray attenuation were then

TABLE 1 Experimental setup with mouse numbers

Procedure and End point [weeks]	0+	1	2	4	8
Destabilization of medial meniscus	$n = 15$[a]	$n = 8$	$n = 8$[bb]	$n = 10$[c]	$n = 9$
Sham (arthrotomy only)	$n = 3$	$n = 5$	$n = 5$[c]	—	$n = 5$
Naïve (age-matched)	$n = 5$[b]	—	—	—	$n = 6$
Mouse age at end point	12 weeks	13 weeks	14 weeks	16 weeks	20 weeks

[a]Contralateral joint missing due to postmortem dissection error (reduced n by 1 for percent difference or normalized data only)—criteria to remove damaged specimens established a priori.
[b]Ipsilateral joint missing due to post mortem dissection error (reduced n by 1 per superscript appearance for imaging and analysis)—criteria to remove damaged specimens established a priori.
[c]Outlier excluded from compartment comparisons (reduced n by 1 for *only* medial bone mineral density distribution measures)—criteria to remove outliers established a priori.

quantified from contrast-enhanced μCT images of the same specimens. Together these quantitative analyses provide a catalog of the post-injury response elicited within both bone and cartilage and the early progression of post-traumatic OA.

2 | METHODS

2.1 | Animals

C57Bl/6J mice were bred in-house and housed in groups of no more than five male mice with one female mouse prior to and after experimental procedures. This reduced aggressive behavior between male animals during the initial post-surgery period, behavior that often results in severe bite wounding on the torso and genitalia. Only male mice were studied because female mice develop a less severe OA after DMM (Ma et al., 2007), as will be elaborated upon in Section 4. Mice were permitted free access to food and water and housed under a standard 12-hr light/dark cycle. Corn-cob bedding was changed at least biweekly, the day before, and immediately after surgery. All surgical procedures were performed in the early afternoon by the same surgeon (J. L.). Each cage was randomly assigned to either DMM, sham, or naïve groups to avoid housing operated mice with uninjured male mice. All procedures were approved by the Rush University Medical Center under IACUC protocol 14-026, and the total mice for each experimental group and end point are summarized (Table 1).

Minimum group sizes ($n \geq 8$ for DMM, $n \geq 3$ for sham) were based on prior work in bone- and cartilage-optimized μCT (Mashiatulla, Moran, et al., 2017; Mashiatulla, Ross, & Sumner, 2017), although 10 were planned per DMM group and up to 5 per sham to allow for any loss during experiments. Losses promptly after DMM (i.e., poor or no recovery from anesthesia) were added to the 0+ week group, resulting in $n = 15$ at that time point, as no tissue content or morphology changes, aside from those directly related to the surgical procedures, were expected to occur within that time frame.

For DMM surgeries, mice were anesthetized by intraperitoneal injection of 60 μl ketamine (100 mg/kg)/xylazine (5 mg/kg) prior to arthrotomy and transection of the medial meniscotibial ligament (Glasson et al., 2007). Operated joints were rinsed with 3 ml sterile saline to remove intra-articular debris or blood before joint capsule and skin were separately sutured. The intra-articular lavage step was established in pilot experiments to reduce the variability in severity of cartilage degeneration among DMM animals. This was likely due to the mitigation of variable early inflammatory phase response expected to occur in response to blood or tissue debris in the joint. Sham procedures were identical except for meniscal detachment. All mice received 60 μl 0.1 mg/kg buprenorphine by intramuscular injection within 24 hr of surgery and were monitored at least daily for pain and distress. Mice were provided additional analgesia (same dosage) when deemed necessary under standard IACUC-approved protocols.

Mice were euthanized using CO_2 asphyxiation followed by cervical dislocation at ~2 hr (0 weeks), 1 week, 2 weeks, 4 weeks, or 8 weeks after DMM (Table 1). The 0-week time point enabled a confirmation of lack of surgical and dissection damage, as well as a comparison age against sham and naïve. Naïve mice were examined at 12 and 20 weeks of age to represent most clearly any age-related changes in bone and/or cartilage parameters in the absence of sham or DMM surgery over the course of the study. Examination of dissected joint surfaces under a dissection microscope (Nikon SMZ1000) confirmed that ligament transection reproducibly resulted in peripatellar medial meniscal and medial joint capsule fibrosis, as well as medial tibial and femoral cartilage lesions (data not shown), consistent with previously reported changes using the DMM model (Glasson et al., 2007). For sham surgeries, medial joint capsule and peripatellar fibrosis were also observed, whereas macroscopic damage to

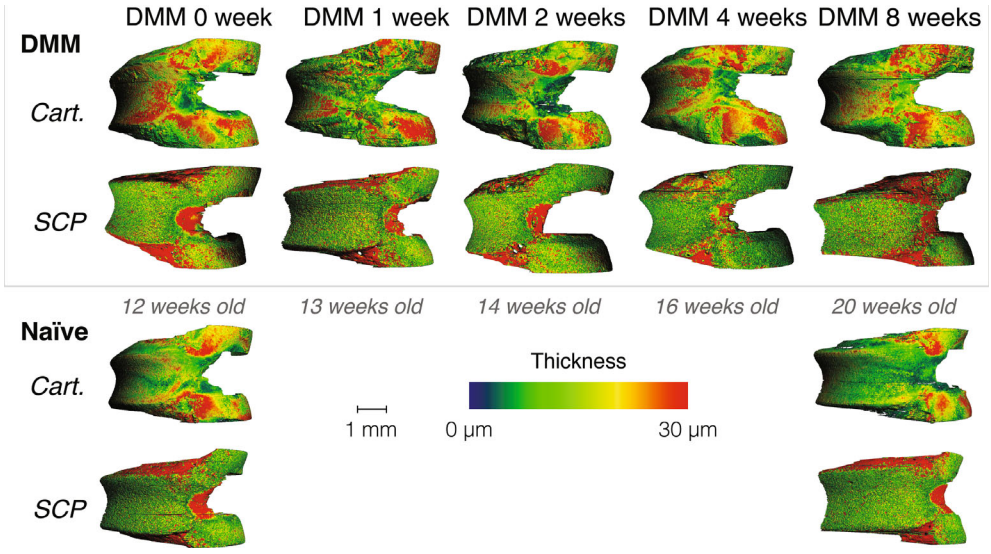

FIGURE 1 Representative cartilage and subchondral bone plate thickness maps derived from µCT images after surgical destabilization of the medial meniscus (DMM). Mice were sacrificed at ~2 hr (0 weeks) and 1, 2, 4, and 8 weeks after DMM surgery, the femurs were scanned by micro-computed tomography (µCT) and compared to femurs from age-matched naïve mice. Scans with and without CA4+ contrast enable the segmentation of non-mineralized articular cartilage and subchondral plate (SCP) regions of interest, respectively. Thickness maps of cartilage (Cart.) and subchondral plate (SCP) are shown for the same representative specimens at each time point after DMM

cartilage and meniscal surfaces was not observed (data not shown). All specimens were fixed in 10% neutral buffered formalin for 2–3 days and then transferred to 70% EtOH until µCT scanning.

2.2 | µCT imaging of subchondral bone plate and cartilage

Both bone- and cartilage-optimized scans, the latter using iodinated contrast agent CA4+ (5,5′-[malonylbis(azanediyl)]bis[*N*1,*N*3-bis(2-aminoethyl)-2,4,6-triiodoisophthalamide]), chloride salt, synthesized, and provided by M. W. G.), were used in this study. µCT imaging with and without CA4+ contrast, permitted the visualization of mineralized tissue and cartilage (Figure 1) and the estimation of cartilage and SCP thickness, respectively, and BMDD. Because contrast agent may concentrate in post-surgical fibrous overgrowth of cartilage surfaces, a result reported in previous mouse models (Chan et al., 2018), and thereby interfere with quantification of contrast-enhanced tissues, we elected to image femora, which demonstrate less severe post-DMM cartilage fibrillation and cartilage loss than tibiae (Glasson et al., 2007).

For bone-optimized scans, femora were wrapped in gauze and immersed in 70% EtOH, for secure placement in the scanner, and the distal 1.8 mm of each femur was scanned (Scanco Medical µCT50, Brüttisellen, Switzerland) at 70 kVp, 57 µA, 1,500-ms integration time, and 2-µm voxel size, as previously described (Mashiatulla, Ross, & Sumner, 2017). The µCT outputs were recorded in linear attenuation units (1/cm). Mineral density calibration was performed at multiple intervals with a wide-range hydroxyapatite (HA) calibration phantom (0–1860 mg HA/cm^3, Roeder Lab, Notre Dame) (Deuerling et al., 2010). Conversion of mineralization from linear attenuation to mineral density and evaluation of BMDD metrics were performed with an in-house MATLAB (R2015b, MathWorks, Natick, MA) script.

For cartilage-optimized scans, the solution osmolality and pH of iodinated contrast agent CA4+, which contains four positive charges and six iodine atoms (Joshi et al., 2009), were maintained at 400 mOsm/kg and 7.4, respectively. Femora were immersed at 4°C in 1 ml of 12 mg iodine/ml CA4+ for at least 40 min, as previously described (Mashiatulla, Moran, et al., 2017). Femora were blotted to remove excess liquid prior to scanning, and samples were affixed at the top of the scanning tube with the distal end of the femur exposed. ~0.5-ml phosphate buffered saline (PBS) was placed in the holder to maintain a humid environment and prevent desiccation. Samples could not be scanned in a solution that still contains contrast agent because the solution itself would attenuate x-rays; nor can samples be placed into CA4+-free solution during imaging because contrast agent will diffuse out of the tissues and into solution due to the drive toward osmotic equilibrium of CA4+ between the tissue and fluid compartments. On the other hand, cationic contrast agent that is ionically

attracted to negatively charged tissue is not expected to diffuse out from a hydrated tissue into a different phase of matter such as air. The distal 1.8 mm of the femur was scanned at 45 kVp, 133 μA, 1,000-ms integration time, and 2-μm voxel size.

2.3 | Contouring of subchondral plate and cartilage

Image slices were acquired in the transverse plane and rotated into the sagittal plane for semi-automatic contouring of SCP and cartilage volumes of interest (Mashiatulla, Moran, et al., 2017). Separately for bone- and cartilage-optimized scans, contours were manually drawn (M. M., blinded to experimental groups) every 20 slices (Scanco Medical V5.15) and morphed to the intervening slices with a Scanco Image Processing Language (IPL) script. Contours for the SCP were drawn along the deep and superficial surfaces of the mineralized tissue, excluding medullary space and articular cartilage. For cartilage scans, initial contours were drawn to include subchondral bone, calcified cartilage, the non-calcified articular cartilage and air, and cartilage-only regions were isolated after further analysis as detailed below.

2.4 | Subchondral plate structure and composition

To characterize the SCP, thickness, volume, and BMDD were calculated from the bone-optimized μCT images. Custom OpenVMS scripts were implemented in Scanco IPL to generate a histogram of grayscale values and calculate tissue thickness and volume by the sphere-fitting method. Frequency distributions from this script were then imported into MATLAB to calculate the mean thickness and total volume. For SCP composition, four BMDD metrics were quantified (mean, *SD*, 5th and 95th percentile values) with a custom MATLAB script (Boskey et al., 2005; Mashiatulla, Ross, & Sumner, 2017; Roschger et al., 2008). Since the BMDD contains values from all the mineralized SCP pixels, the nature of the distribution was quantified by *SD* and percentiles. The 5th and 95th percentiles indicate the spread of values into the tails of the BMDD and can change with experimental groups, even if mean and *SD* do not, because the BMDD may not be symmetric. The characterization of these two percentiles helps to provide context to changes in SD, as accumulation of 5th may be due to inhibited mineralization, while accumulation of 95th could be due to accumulation of hypomineralized region, prolonged secondary mineralization, or large amounts of cement lines (Roschger et al., 2008).

2.5 | Cartilage structure and composition

Cartilage thickness, total volume, and mean attenuation were quantified from the cartilage-optimized μCT scans. The histogram for cartilage scans showed three distinct peaks: calcified cartilage and bone, articular cartilage, and air (Mashiatulla, Moran, et al., 2017). Linear attenuation threshold values of -2 and 4 cm^{-1} sufficiently separated calcified tissues and air from the cartilage for most specimens. Cartilage was segmented as the tissues with attenuation within these threshold values, and the segmented region was used to calculate cartilage thickness and volume. Notably, the magnitude of attenuation is not considered for measurement of cartilage thickness and volume, so long as it falls within these threshold values for calcified tissues and air. Although CA4+ equilibrates preferentially into negatively charged tissues, it nonetheless will enhance attenuation in neutral-charged tissues (e.g., no GAG but containing collagen) to greater than that of air (Bansal, Stewart, et al., 2011). After thresholding, the mean attenuation of articular cartilage was also calculated from the distribution and is a correlate of fixed (negative) charge density, the majority of which is attributable to GAG content (Lakin et al., 2013; Mashiatulla, Moran, et al., 2017). The OpenVMS scripts and MATLAB code for SCP morphology were also applied to the contoured cartilage to calculate average thickness and total volume.

2.6 | Analyses by compartment

To further distinguish the regional relationship of morphology or composition changes, both bone- and cartilage-optimized μCT scans were divided into the medial condyle, lateral condyle, and trochlear groove. Selected analyses for global metrics of SCP and cartilage as described above were repeated for the medial, lateral, and patellar compartments of the operated femora.

2.7 | Data calculation and statistical evaluation

To control against confounders including cage effects and individual mouse differences, global parameters in the operated leg were normalized against those of the contralateral leg as a percent difference with respect to contralateral ([operated–contralateral]/contralateral). Normalized compartment data are presented as the compartment-specific operated joint value divided by the contralateral global value. Notably, normalization against the

contralateral leg may obscure systemic effects of the surgery (e.g., systemic inflammation, gait changes), so interpretation of differences among treatment groups and time points must consider both raw and normalized values.

Statistical analyses were performed (D. C., M. P.) using R (R Development Core Team, 2010) implemented in R Studio (RStudio Team, 2020) with ggplot2 (Wickham, 2016) and other packages, with statistical significance was defined at $\alpha = .050$. Anderson–Darling tests were used to confirm normality within each experimental subset, and sample variances were tested among groups using Levene's median test. The effect of progression (i.e., time point) was tested among operated legs using a one-way analysis of variance (ANOVA) or a Kruskal–Wallis rank sum test for non-normal distributions or unequal sample variances. Significant effects were probed with post hoc Tukey's honest significant difference or Dunn's test, respectively. Time point or age-matched groups (i.e., DMM vs. sham at a specific time point, 12- and 20-week-old naïve animals) were compared by Welch's unequal variance *t* test, while operated and contralateral limbs were compared with paired two-tailed *t* tests. Cross-correlations were performed using Pearson's correlation among all parameters, inclusive of all treatments and time points, on the operated leg for DMM and sham and the right leg for naïve mice.

3 | RESULTS

3.1 | Cartilage morphology and contrast-enhanced attenuation

CA4+ contrast-enhanced μCT data for cartilage thickness and volume, as well as mean attenuation at ~2 hr (0+ weeks) and 1, 2, 4, and 8 weeks was determined (Figure 2). Since CA4+ contrast agent partitions preferentially to tissues with high concentrations of negatively charged GAGs (Bansal et al., 2010), mean tissue attenuation of x-rays correlates to GAG content and mechanical properties of cartilage (Lakin et al., 2016).

Cartilage parameters were not significantly altered at 2 hr after surgery when compared to age-matched naïve, supporting the absence of surgical or dissection damage to the tissues. However, a time-point effect after DMM was significant for cartilage thickness ($p = .01$) and mean attenuation ($p = .006$), with significant post-hoc differences after 2 and 8 weeks, respectively. Cartilage thickness increased and peaked at 2 weeks ($p = .024$) but was the same as 0-week levels at 4 to 8 weeks post-DMM. Mean attenuation was significantly lower at 2 weeks ($p = .016$) and remained low up to 8 weeks post-DMM ($p = .023$). Similar time-point trends were observed but not statistically significant for cartilage volume ($p = .098$). Interestingly, cartilage thickness ($p = .012$) and volume ($p = .001$) at 8 weeks post-DMM were greater than, but attenuation ($p < .001$) was less than, those of age-matched naïve mice. Normalization of cartilage metrics to the contralateral joint (Figure 2c) did not appreciably change the trends or significance.

3.2 | Bone morphology and mineralization

Bone-optimized μCT scans were used for SCP morphology and BMDD (Mashiatulla, Ross, & Sumner, 2017) at 0+, 1, 2, 4, and 8 weeks after DMM, and contralateral and normalized data were compared (Figure 3). Two hours post-DMM, SCP thickness and volume were not different compared to naïve age-matched controls, whereas BMDD mean ($p < .001$) was greater in DMM group in both operated ($1{,}023 \pm 55$ mg HA/cm^3) and contralateral ($1{,}041 \pm 43$ mg HA/cm^3) legs than naïve (851 ± 16 and 868 ± 16 mg HA/cm^3, right and left legs). Significant time point effects were found with BMDD mean ($p = .035$), SCP thickness ($p < .001$), and SCP volume ($p = .001$) (Figure 3), as well as BMDD *SD* ($p = .048$), 5th percentile ($p = .004$), and 95th percentile ($p = .048$) (Figure 4). Specifically, SCP thickness and volume were least at 2 weeks with a return to or greater than 0-week levels by 8 weeks. Mean BMDD 8 weeks post-DMM ($1{,}033 \pm 68$ mg HA/cm^3) was significantly greater than age-matched naïve mice (922 ± 11 mg HA/cm^3, $p = .001$).

3.3 | Changes in medial and lateral femoral compartments and patellar groove

Analyses by compartment were performed for cartilage thickness and attenuation (Figure 5) and SCP thickness and BMDD mean (Figure 6). Cartilage thickness was not changed in any compartment (medial $p = .128$, lateral $p = .309$, patellar $p = .094$, Figure 5). Significant time point effects in cartilage mean attenuation were found in medial ($p = .045$) and patellar ($p = .041$) but not lateral compartments ($p = .454$), with significant post hoc comparisons shown (Figure 5).

BMDD mean and SCP thickness were greater in the lateral and medial compartments than the patellar compartment, within all treatment groups and post-surgery time points. Trends for global changes to SCP parameters after DMM (Figure 3) were generally reflected in the compartment analysis. SCP thickness was altered in the lateral ($p < .001$), medial ($p = .037$), and patellar ($p < .001$) compartments (Figure 6). BMDD means

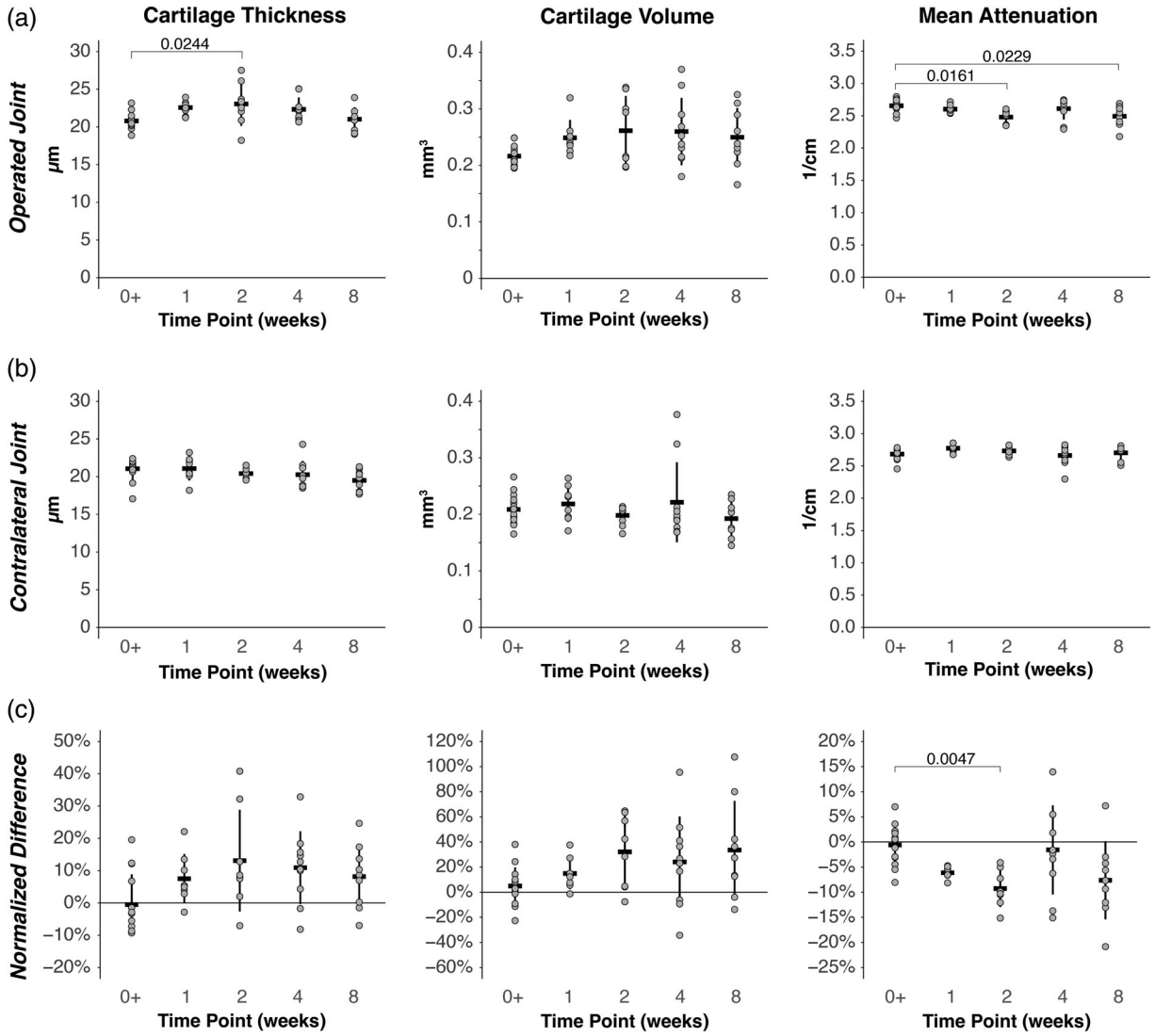

FIGURE 2 Effect of destabilization of the medial meniscus (DMM) surgery on cartilage of the distal femora. Cartilage morphology and mean attenuation were determined from contrast-enhanced micro-computed tomography (μCT) of the operated (a) and contralateral (b) joints. The difference between operated and contralateral joints were normalized by the contralateral values (c). Data are plotted by individual animals (gray circles) and group mean (black bar), with *SD* (thick line). Significant between-group differences are highlighted by the horizontal brackets with *p* values indicated

showed significant time point effects after DMM in lateral ($p = .012$) but not medial ($p = .118$) or patellar ($p = .105$) compartments (Figure 6).

3.4 | Effect of sham surgery on cartilage and SCP morphology and matrix changes

Naïve mice generally showed significant increases in SCP BMDD mean ($p < .001$) and thickness ($p = .017$) but not in other SCP or cartilage parameters, between 12- and 20-weeks of age. However, both operated and contralateral parameters from 8-week sham mice showed some significant differences from age-matched, 20-week-old naïve mice (Table S1). Representative μCT images of cartilage and mineralized tissues from the femora of sham operated joints are shown (Figure 7), with cartilage (Figure 8) and SCP (Figure 9) parameters calculated for operated and contralateral joints.

Cartilage parameters in sham showed a significant time-point effect (Figure 8), including in volume ($p = .001$), attenuation ($p < .001$), and contralateral-normalized thickness ($p = .015$). Post hoc comparisons showed that contralateral-normalized cartilage thickness was significantly greater at 1-week than 0-week, 2-week, and 8-week post-sham (Figure 8). At 8 weeks post-sham, the mean cartilage attenuation was significantly less than ($p < .001$) age-matched naïve mice (Table S1). Significant time point effects were observed in the sham-operated joint for SCP thickness and volume (Figure 9). After

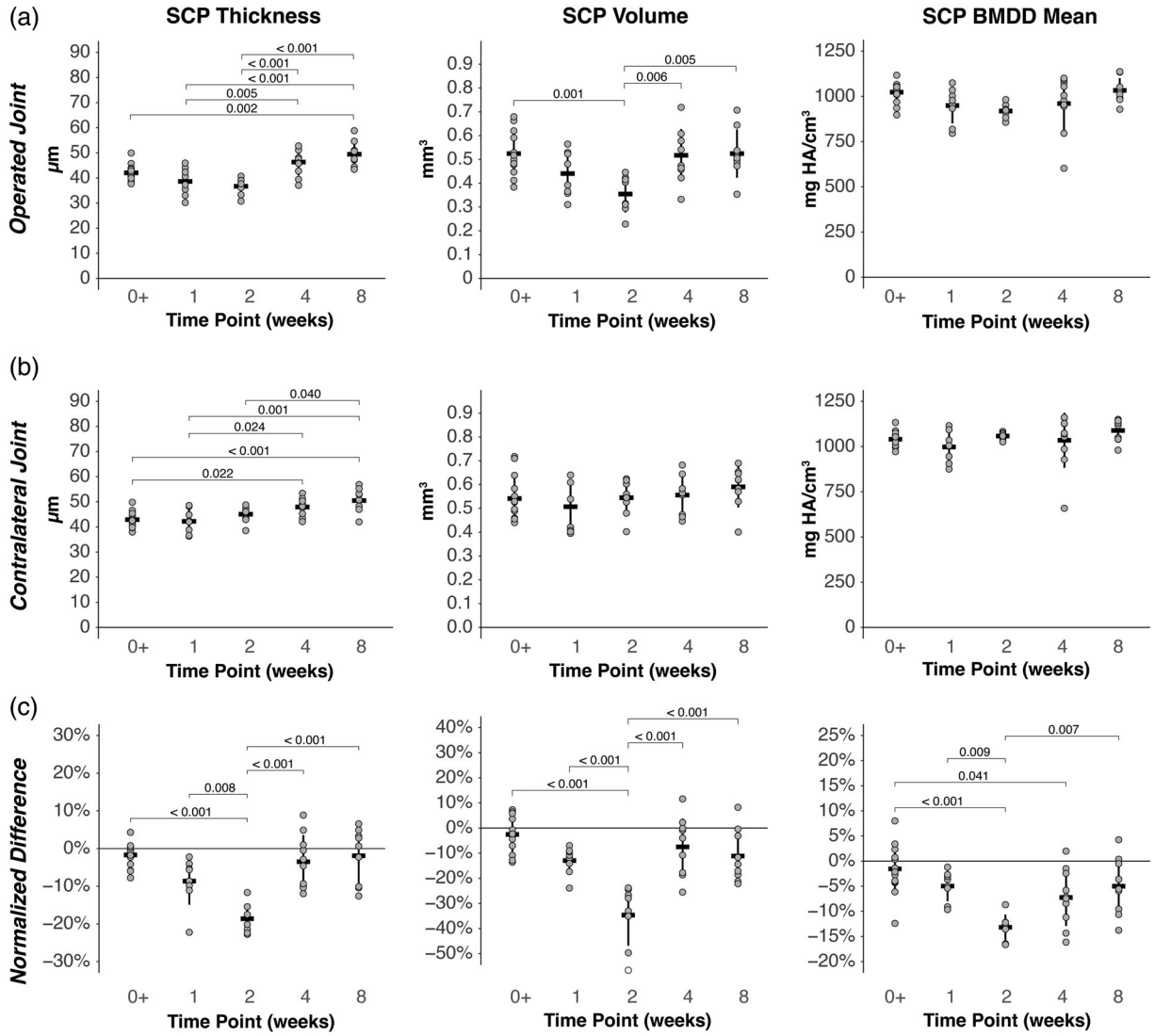

FIGURE 3 Effect of destabilization of the medial meniscus (DMM) surgery on subchondral plate of the distal femora. Subchondral plate (SCP) morphology and bone mineral density were evaluated from micro-computed tomography (μCT) without use of a contrast agent. Thickness, volume, mean attenuation, and mean of the bone mineral density (BMD) distribution were calculated for the operated (a) and contralateral (b) joints. The difference between operated and contralateral joints were normalized by the contralateral values (c). Data are plotted by individual animals (gray circles) and group mean (black bar), with *SD* (thick line). Significant between-group differences are highlighted by the horizontal brackets with *p* values indicated

contralateral normalization, significant time point effects were found also in BMDD mean ($p = .009$), thickness ($p = .001$), and volume ($p = .003$), with all parameters decreasing by 2 weeks but returning to 0-week levels by 8 weeks (Figure 9).

3.5 | Differences between DMM and sham surgery effects on cartilage and subchondral plate

Comparisons of DMM mice (Figures 1–3) to sham (Figures 7–9) showed differences in cartilage parameters only at 1 week after DMM (Table S2). In the operated joint, DMM mice showed significantly thinner cartilage ($p = .022$) compared to sham. After contralateral normalization, DMM mice also had significantly less cartilage volume ($p = .007$) and mean attenuation ($p = .019$) than sham at 1 week after surgery. BMDD metrics in DMM joints were generally significantly different from sham (Table S2). SCP thickness differed significantly only at 8 weeks ($p = .026$). However, once SCP metrics were normalized to contralateral (Table S2), significant differences between DMM and sham remained only at 1 and 2 weeks for BMDD mean and 5th and 95th percentiles.

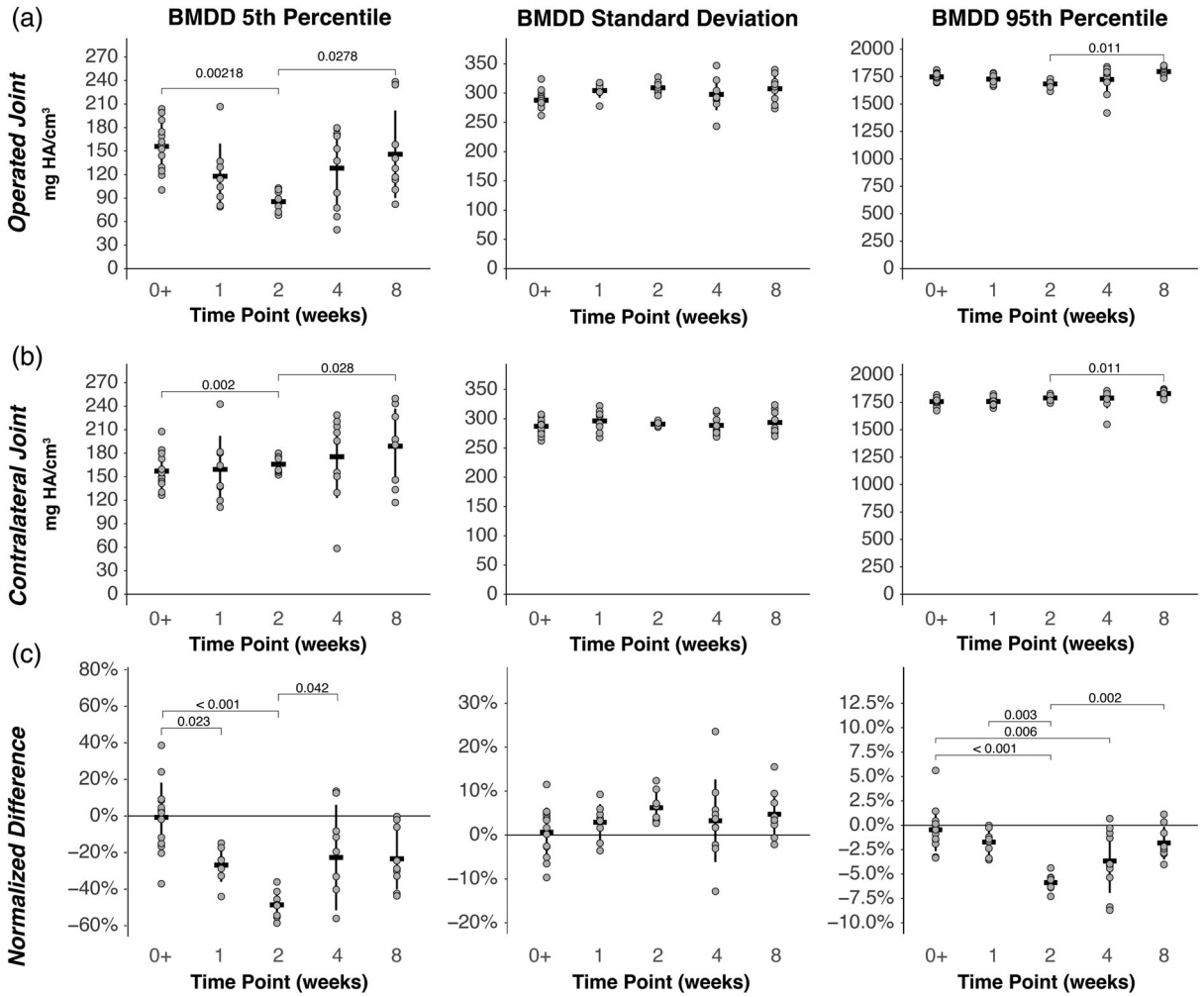

FIGURE 4 Destabilization of the medial meniscus (DMM) significantly altered the spread of the bone mineral density distribution (BMDD). *SD* and 5th and 95th percentiles were measured from the bone mineral density distribution (BMDD) after DMM in the operated (a) and contralateral (b) distal femora to determine whether the changes in bone mineral density represented only a shift in values (mean) or had effects in other measures of the distribution throughout mineralized tissues. Time effects after DMM were significant for 5th percentile ($p = .004$), *SD* ($p = .048$), and 95th percentile ($p = .022$) of the BMDD. (c) Time effects remained significant after normalization to contralateral leg for the 5th and 95th percentiles (both $p < .001$) but not the *SD* ($p = .306$). Significant post hoc comparisons are shown with their *p* values. Data are plotted by individual animals (gray circles) and group mean (black bar), with *SD* (thick line)

3.6 | Subchondral plate and cartilage parameter relationships

SCP and cartilage parameters in the operated leg (a–c) and contralateral-normalized (d–f) parameters significantly cross-correlated within naïve, sham, and DMM groups (Figure 10 and Table S3). As defined in Section 2, contralateral-normalized parameters are the parameters from the operated leg, normalized against those of the contralateral leg as a percent difference with respect to contralateral ([operated–contralateral]/contralateral). This approach was used to control against confounders including cage effects and individual mouse differences, to which a cross-correlation analysis among bone and cartilage parameters may be particularly sensitive. Notably, cartilage thickness with DMM was negatively and significantly correlated to BMDD mean as well as SCP thickness and volume. Cartilage mean attenuation positively correlated to BMDD fifth percentile and SCP volume but only in contralateral normalized data sets. BMDD metrics were generally positively correlated with SCP thickness and volume, although the *SD* of BMDD values was negatively correlated.

4 | DISCUSSION

In this study, we report CA4+-enhanced μCT and bone-optimized μCT being used together for the first time to characterize the time course of cartilage and SCP changes

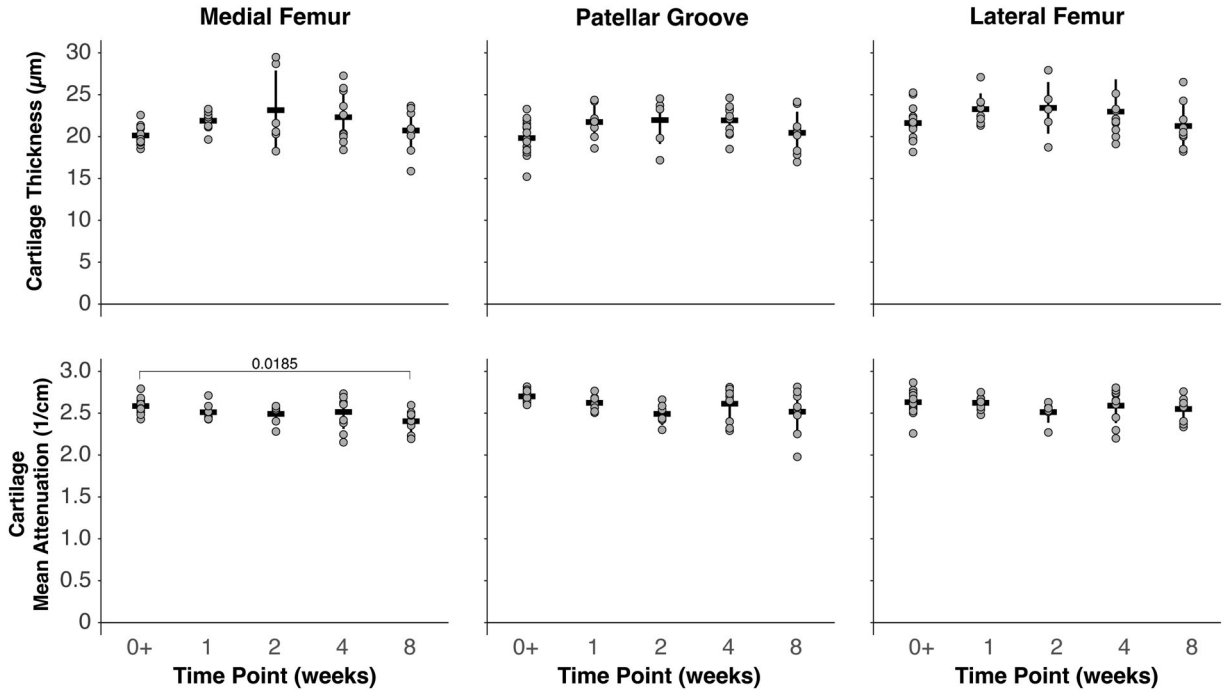

FIGURE 5 Thickness and mean attenuation of medial and lateral femoral compartment and patellar groove cartilage. Cartilage thickness and mean attenuation for the medial, patellar, and lateral compartments were measured after destabilization of the medial meniscus (DMM). Only one post hoc pairwise comparison—medial mean attenuation between 0 and 8 weeks—reached significance. Data are plotted by individual animals (gray circles) and group mean (black bar), with *SD* (thick line). Significant post hoc comparisons are shown with brackets and labeled with their *p* values

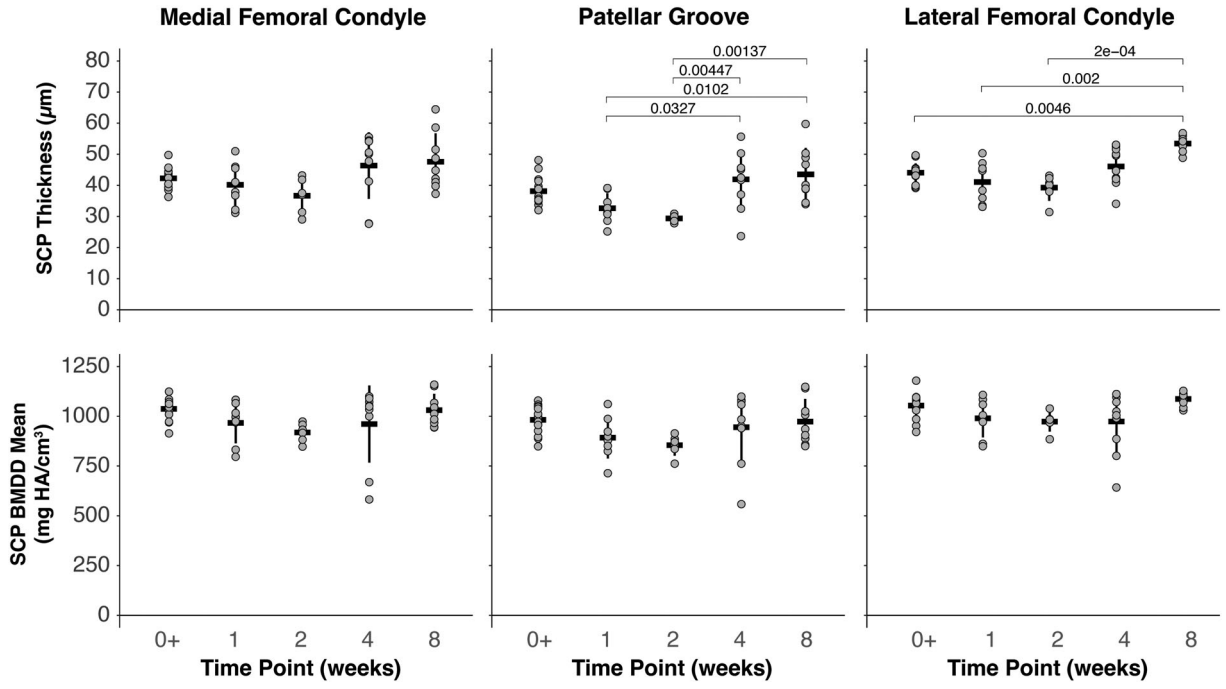

FIGURE 6 Subchondral plate thickness and mean of the bone mineral density distribution (BMDD) of medial and lateral femoral compartments and patellar groove. Subchondral bone plate thickness and BMDD mean were calculated for each compartment. Significant post hoc comparisons are indicated with p values. Data are plotted by individual animals (gray circles) and group mean (black bar), with *SD* (thick line). Significant post hoc comparisons are shown with brackets and labeled with their *p* values

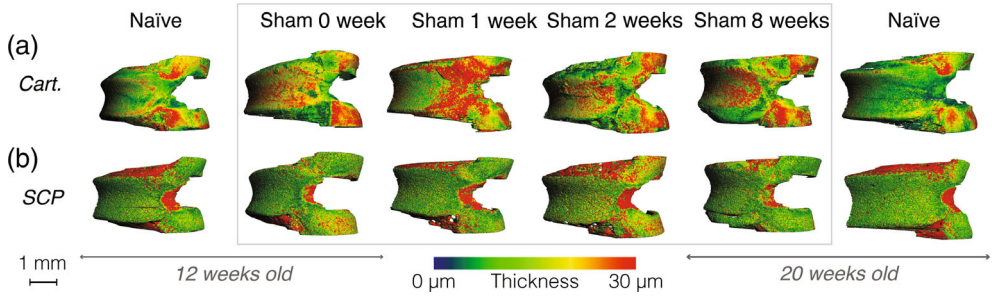

FIGURE 7 Representative cartilage (a) and subchondral bone plate (b) thickness maps derived from micro-computed tomography (µCT) after sham surgery and in age-matched naïve mice. Mice were sacrificed at ~2 hr (0 weeks) and 1, 2, and 8 weeks after sham surgery, prepared for imaging with contrast-enhanced µCT. Age-matched naïve joints (Figure 1) are shown again for comparison. Contrast-enhanced µCT permitted measurements of non-mineralized cartilage and subchondral plate (SCP) thickness as mapped here, in addition to other tissue morphology parameters and matrix content

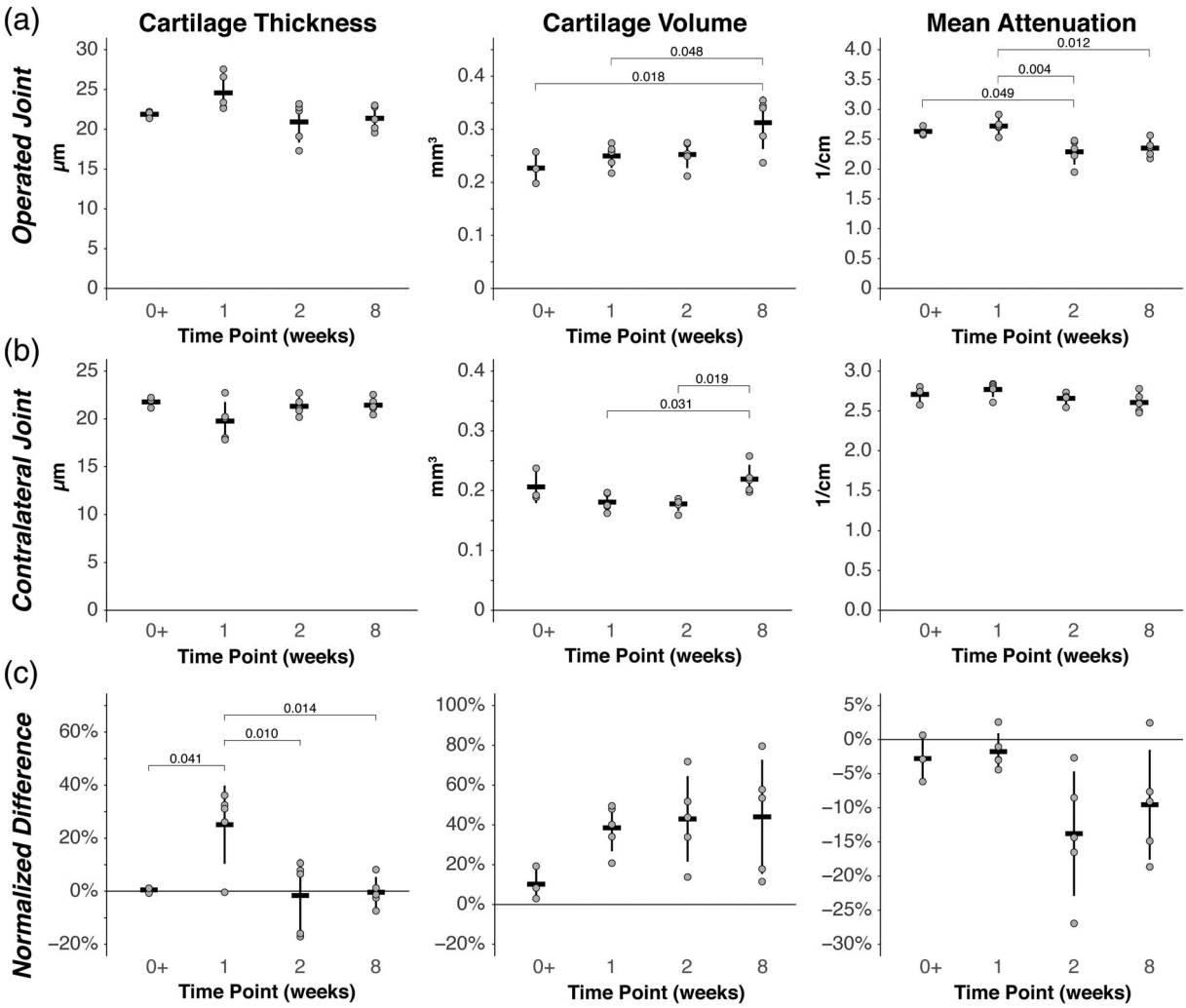

FIGURE 8 Effect of sham surgery on cartilage of the distal femora in sham-operated animals. Cartilage parameters were measured in the sham-operated (a) and contralateral (b) legs, and the difference was normalized by the contralateral values (c). Cartilage thickness, but not cartilage volume or mean attenuation was significantly altered with sham operation ($p = .006$), increasing at 1 week returning to 0-week levels by 2 weeks. In the contralateral sham leg, significant effects were found in cartilage volume ($p = .0122$) but not cartilage thickness or attenuation. Data are plotted by individual animals (gray circles) and group mean (black bar), with *SD* (thick line). Significant post hoc comparisons are shown with brackets and labeled with their p values

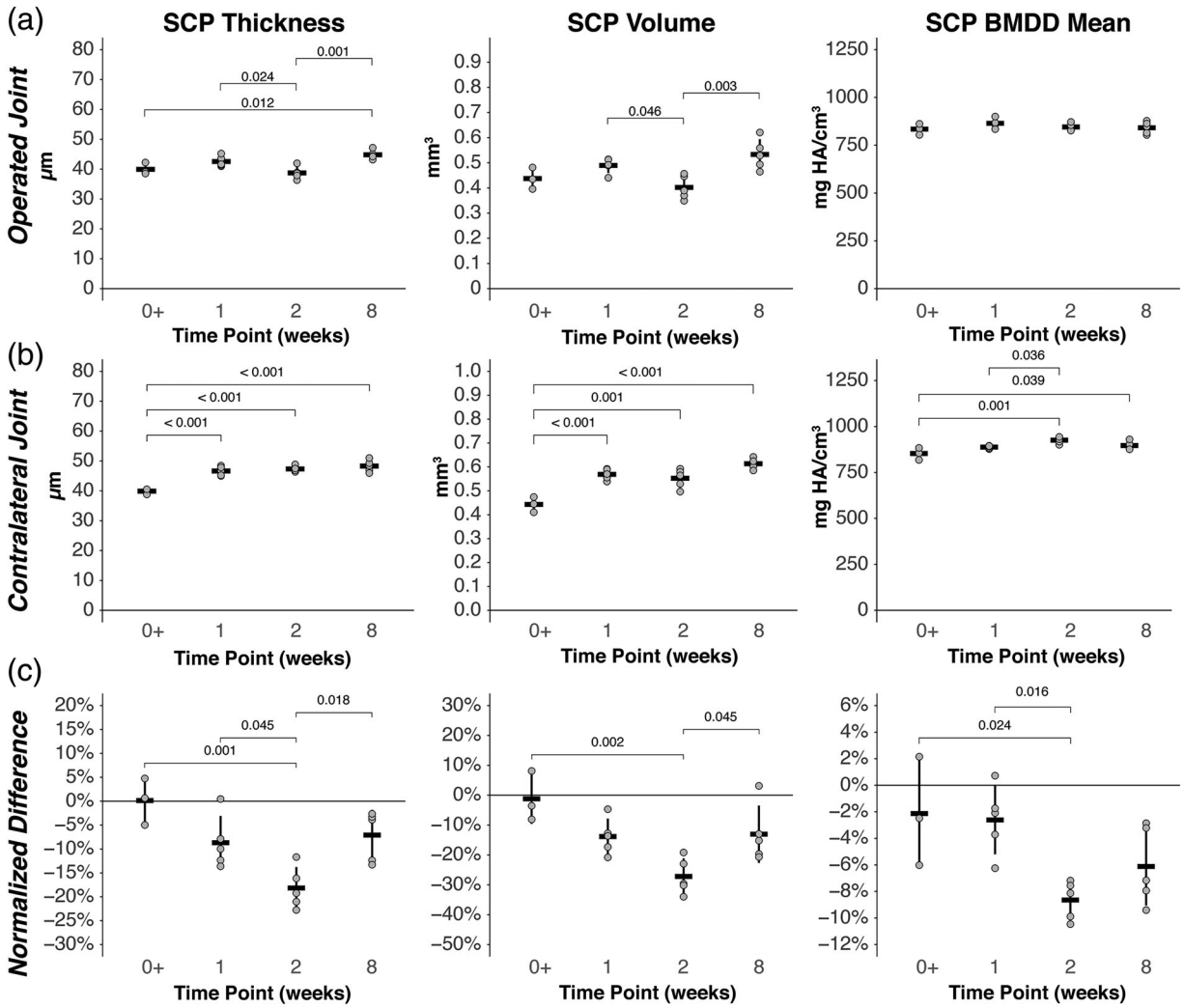

FIGURE 9 Effect of sham surgery on subchondral plate of the distal femora in sham-operated animals. Subchondral plate (SCP) parameters were measured in the sham-operated (a) and contralateral (b) legs, and the difference was normalized by the contralateral values (c). SCP thickness ($p < .005$) and volume ($p = .004$), but not mean bone mineral density (BMD), showed significant time point effects in operated sham legs. Contralateral sham legs showed significant time point effects in SCP thickness ($p < .005$), SCP volume ($p < .005$), and mean BMD ($p = .001$). Data are plotted by individual animals (gray circles) and group mean (black bar), with *SD* (thick line). Significant post hoc comparisons are shown with brackets and labeled with their *p* values

in the DMM model of murine post-traumatic OA. This study demonstrates the application of both bone- and cartilage-optimized μCT to quantitate and analyze simultaneous changes in tissue content and morphology in the femur, although these methods can be broadly applied to other osteochondral compartments of the stifle and indeed other synovial joints in any preclinical model. The overall imaging outcomes of this study show significant changes early, within 2 weeks, after DMM surgery for the SCP parameters more than cartilage parameters. Significant correlations exist between cartilage and SCP parameters, in addition to those expected within each tissue. Notably, there are also more significant pairings among the SCP and cartilage parameters with DMM and sham than naïve. This finding suggests that cartilage-bone crosstalk may play a greater role in OA joints than healthy ones, which observations of increased tissue matrix permeability after DMM (Pan et al., 2012) surgery support.

Contrast-enhanced μCT of murine femurs after DMM surgery enables the quantification of cartilage and SCP changes. Assessment of both SCP and cartilage changes in the same imaged joints permits cross-correlation of these metrics across a range of treatments and time-points. Since significant changes in SCP thickness and BMDD associate with continued skeletal maturation between 12 and 20 weeks in the mice used in this study, we report outcomes normalized to contralateral in addition to data only from operated legs.

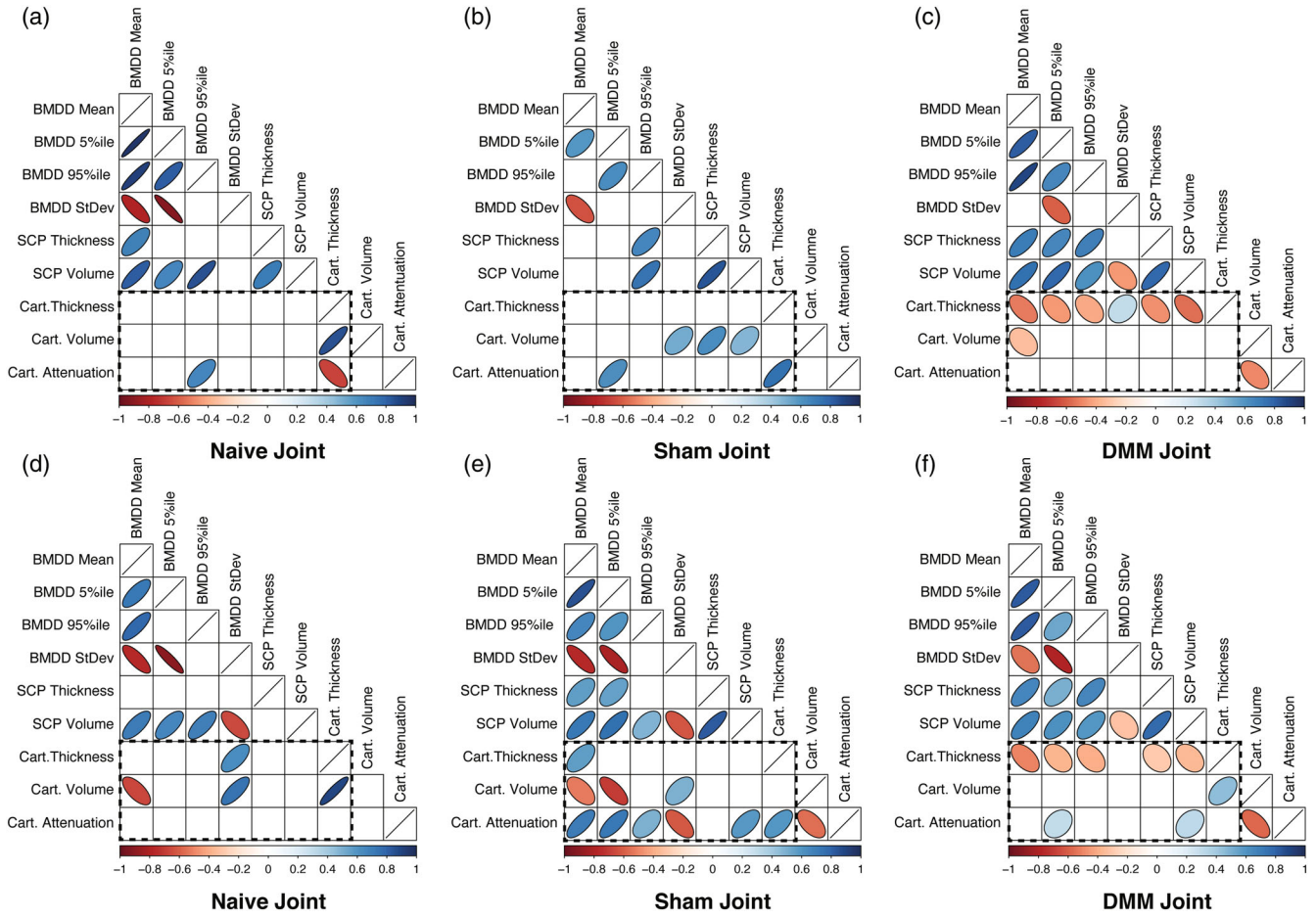

FIGURE 10 Cross-correlation among bone and cartilage parameters demonstrated significant associations among micro-computed tomography (μCT)-derived metrics after DMM. μCT permitted the global measurement of bone mineral density distribution (BMDD) metrics, cartilage and subchondral plate (SCP) morphology, and cartilage mean x-ray attenuation after CA4+ contrast, which can be used to estimate proteoglycan content. Cross-correlation (whose coefficients range from −1 to 1) among variables in the naïve (a,d), sham (b,e), operated (c,f) leg for DMM identified the slope and strength of significant correlations (ellipses shown only for $p < .05$) in operated joint (a–c) and contralateral-normalized (d–f) values. The eccentricity of ellipses is scaled to the correlation value, such that narrower ellipses indicate a greater absolute value of the significant cross-correlation coefficient. Bone-cartilage correlation pairs are indicated within the thick dashed black outlines

Normalization by the contralateral joint changes the significance of relationships among some time points or treatment groups. These observations suggest the need for better approaches to controlling for individual mouse and cage variations without obscuring systemic, contralateral, and arthrotomy effects. While contralateral limbs are valuable for comparison across animals that may vary in size and biological responses, the normalization approach may obscure systemic changes, including inflammation. With the potential for altered biomechanics and behavior after surgery, systemic effects cannot be inferred from the contralateral limb alone.

The earliest significant changes in the femora post-DMM at 2 weeks include greater cartilage thickness but less cartilage mean attenuation, SCP volume, and BMDD mean compared to 0+ weeks. Although the reduction in SCP thickness is not significant in the 1- and 2-week post-DMM groups, the thinning of the SCP at early time points—followed by sclerosis at later stages of disease—has been observed in several previous studies (Burr & Gallant, 2012). SCP thinning is consistent with the increased bone remodeling that is associated with cartilage degeneration (Muehleman et al., 2002) and early post-traumatic OA (Ziemian et al., 2021) and targeted to mitigate disease progression. Eight weeks after DMM, SCP thickness, but not SCP volume or BMDD mean, is significantly greater than 0+ weeks. Indeed, in similarly aged mice, SCP thickness increased 4 weeks after DMM in the medial posterior femoral condyle, but not medial anterior nor lateral condyles (Jia et al., 2018). However, the age and growth trajectory of mice in this study may partially explain greater SCP thickness but also the lack

of reduction of BMDD mean at 8 weeks. SCP thickness and BMDD mean are both significantly greater in naïve mice at 20 weeks of age, compared to 12 weeks old. Interestingly, normalization to the contralateral joint results in significant differences in BMDD mean in 2 and 4 weeks post-DMM groups, suggesting that either variations in BMDD of individual mice or systemic BMDD effects of DMM may mask some effects within the injured joint. Others have reported that epiphyseal bone mineral density was not appreciably changed at 2 weeks but was greater in the medial tibial plateau (but not lateral tibial plateau nor femoral condyles) at 5 and 10 weeks after DMM surgery compared to time-point matched sham (Fang et al., 2018). However, that prior study did not examine the SCP, potentially indicating that SCP and cartilage changes may be more sensitive to early changes after joint injury.

Prior work has evaluated the relationship between contrast enhancement by CA4+ and biochemical and biomechanical properties of murine tibial plateau cartilage in healthy joints (Lakin et al., 2016). In this study, although cartilage parameters change with time after DMM, only 2-week post-DMM values reach statistical significance compared to the 0-week time point. Cartilage mean attenuation is significantly less at 2 weeks after DMM, mirroring the loss of GAG seen with histology after DMM (Fang et al., 2018; Glasson et al., 2007). Cartilage thickness is also significantly greater at 2 weeks after DMM, suggesting potential swelling of cartilage early after joint injury, such as that seen in partial meniscectomy in a rabbit model (Calvo et al., 2004). Taken together, the greater variance in mean attenuation values within cartilage at 4 and 8 weeks after DMM and the apparent swelling behavior may be explained by the increased time required for CA4+ equilibration into tissues with reduced proteoglycan content (Bhattarai et al., 2021).

Statistically significant compartment-specific changes in the femur (medial, lateral femoral condyles or patellar groove) follow the timing of changes in the global metrics for both cartilage and SCP. Future studies to optimize imaging and image processing for the tibial compartment may better delineate early cartilage composition changes, since the tibia appears to display more severe post-DMM cartilage fibrillation and loss with histopathology (Glasson et al., 2007). Cellular changes (Pritzker et al., 2006) occur by 3 days, with articular surface damage at 7 days, in the medial tibial plateau with DMM (David et al., 2017). Taken together, the changes observed at 2 weeks that appear to recover by 8 weeks may be a combined effect of SCP or bone remodeling after DMM and continued skeletal maturation and growth of the mice between 12 and 20 weeks of age. Although the age range used in this study is typical for DMM studies (9–12 weeks at surgery; Bateman et al., 2013; Das Neves Borges et al., 2014; David et al., 2017; Doyran et al., 2017), the progression of cartilage and SCP changes may differ if DMM were instead initiated in skeletally mature mice.

Importantly, sham surgery, which includes arthrotomy without physical detachment of the meniscus, also results in significant changes after 8 weeks in both SCP and cartilage morphology and composition, compared to the contralateral and age-matched naïve. These findings highlight an inherent limitation of surgical models, wherein the effect of soft tissue healing responses following arthrotomy likely contributes both locally and systemically to joint remodeling responses. For example, macrophage and monocyte responses after DMM surgery include greater CD64, CD206, and iNOS expression (M1 macrophage markers) in both DMM and sham limbs, compared to naïve (Utomo et al., 2021). In addition, similar inflammatory and fibrotic pathway expression profiles were observed in both sham surgery and joint injury in wild-type mice (Chan et al., 2015).

A limitation for cartilage-specific imaging with μCT is likely related to the contrast agent, which generally partitions to negatively charged tissues rather than more specifically targeting articular cartilage. Contrast agent could also concentrate in post-surgical fibrous overgrowth of cartilage surfaces, as previously reported for a cartilage injury model (Chan et al., 2018). For this reason, we opted to evaluate femora rather than tibiae in this study, despite the earlier appearance of histological changes in the tibial plateau described in prior DMM studies (Glasson et al., 2007). The cartilage surfaces of the tibial compartment are difficult to dissect lean of adherent tissues from the meniscal and periosteal margins, a particular concern with DMM since fibrous overgrowth on the medial side—originating from the surgical detachment of the medial meniscus—is observed during dissection. Inclusion of these fibrous tissues, which contain anionic GAGs and glycoproteins, with CA4+ contrast enhancement would likely have biased cartilage volume and mean attenuation measurements. An improved approach of using multiple contrast agents for μCT (Bhattarai et al., 2020) or the use of more specific extracellular matrix markers in other imaging modalities (Hui Mingalone et al., 2018; Lim et al., 2015) may improve sensitivity to detection of cartilage-specific morphometric changes in joint injury models. These or other improvements may be necessary before contrast-enhanced μCT can be used in intact whole joints to evaluate changes in all joint tissues with post-traumatic OA progression. In the same context, 3D and longitudinal imaging could also enable greater sensitivity to the changes in the whole

joint after injury or surgery, providing internal controls for each animal without the need for normalization to contralateral. Use of other imaging tools not discussed here may also provide additional insight (as reviewed by others; Lim et al., 2020; Drevet et al., 2022) by complementing contrast-enhanced μCT.

In addition, female mice are likely to show different progression of cartilage and SCP changes, based on work that demonstrated less severe OA development after DMM (Ma et al., 2007). Notably, that study showed a role for sex hormones in the progression of OA, in that a more severe joint pathology occurred in ovariectomized (i.e., estrogen-deficient) female animals and a less severe OA in orchiectomized (i.e., testosterone-deficient) males. Although ovariectomy prior to DMM may be useful to model OA in older, potentially post-menopausal women, considered to be at greater risk for OA than men, the above study utilized mice at 10 weeks of age, prior to skeletal maturity, which is considered to be ~16 weeks of age (Ferguson et al., 2003; Somerville et al., 2004). Furthermore, ovariectomy induces bone loss, independent of DMM or other injury models, that varies by both mouse strain and skeletal location (Bouxsein et al., 2005) and would generate confounding factors affecting bone and cartilage remodeling outcomes in the DMM model. Although housing with a single female mouse reduced cases of aggressive and other potentially stressful behaviors, this study did not measure differences in sex hormone levels, which could be confounding variables in addition to the physical and stress responses to aggression and its consequences. Notably, gross joint pathology performed in our study after euthanasia showed comparable DMM-associated changes as prior studies performed in male mice not housed with female mice (Li et al., 2011). Nonetheless, effects of sex as a biological variable, sex hormones, and their interaction with skeletal age could be further investigated in murine OA models, to provide the role of such variables in the pathogenesis of human OA.

In this study, we used μCT of mineralized tissues in the SCP and contrast-enhanced μCT of articular cartilage to analyze femoral bone and cartilage from mice after DMM or sham surgeries. We quantified the morphology and composition of both SCP and cartilage in this model of post-traumatic OA. With increasing appreciation of the importance of subchondral bone remodeling and its effect on cartilage metabolism in OA (Adebayo et al., 2017; Bailey et al., 2021; Fang et al., 2018; Jung et al., 2018; Nagira et al., 2020; Pan et al., 2012), further development of volumetric imaging, such as contrast-enhanced μCT, capable of imaging mineralized and soft tissues within the joint is essential to advancing our understanding of this whole joint disease.

AUTHOR CONTRIBUTIONS

Deva D. Chan: Data curation (equal); formal analysis (equal); investigation (supporting); methodology (supporting); validation (equal); visualization (equal); writing – original draft (supporting); writing – review and editing (lead). **Maleeha Mashiatulla:** Conceptualization (equal); data curation (lead); formal analysis (equal); investigation (lead); methodology (equal); visualization (supporting); writing – original draft (lead); writing – review and editing (supporting). **Jun Li:** Data curation (supporting); formal analysis (supporting); investigation (supporting); methodology (supporting); resources (supporting); writing – original draft (supporting); writing – review and editing (supporting). **Ryan D. Ross:** Data curation (supporting); formal analysis (supporting); investigation (supporting); methodology (supporting); resources (supporting); writing – review and editing (supporting). **Meghana Pendyala:** Data curation (supporting); formal analysis (equal); visualization (equal); writing – review and editing (equal). **Amit Patwa:** Methodology (supporting); resources (supporting); writing – review and editing (supporting). **Mark W. Grinstaff:** Conceptualization (supporting); methodology (supporting); resources (equal); writing – review and editing (supporting). **Anna Plaas:** Conceptualization (equal); funding acquisition (supporting); resources (equal); supervision (equal); visualization (supporting); writing – original draft (supporting); writing – review and editing (supporting). **D. Rick Sumner:** Conceptualization (equal); formal analysis (supporting); funding acquisition (lead); investigation (supporting); methodology (supporting); resources (lead); software (supporting); supervision (lead); visualization (supporting); writing – original draft (supporting); writing – review and editing (supporting).

ACKNOWLEDGMENTS

The authors acknowledge research staff at the Rush University MicroCT and Histology Core and members of the Grinstaff Laboratory at Boston University.

FUNDING INFORMATION

This work was performed at the Rush University MicroCT and Histology Core, on equipment purchased through National Institutes of Health Shared Instrumentation grant 1S10RR027980 (PI: D. Rick Sumner). Some authors were supported directly and/or indirectly through the Katz-Rubschlager Endowment for Osteoarthritis Research (Anna Plaas) and National Science Foundation Awards 1944394 and 2149946 (PI: Deva D. Chan, Meghana Pendyala). The funders had no role in study design, data collection and analysis, decision to publish, or preparation of the manuscript.

CONFLICT OF INTEREST

The authors have no direct conflicts of interest to report.

DATA AVAILABILITY STATEMENT

Metrics derived from the image data are posted in a publicly available repository at https://doi.org/10.7910/DVN/FJCM6R. However, due to the large imaging data sets used in this study, the image data are not available in a public repository. Interested parties should contact the corresponding author for data, which will need to be recovered from archive prior to availability for file transfer.

ETHICS STATEMENT

All procedures in living mice described herein were approved by and conducted at Rush University Medical Center under IACUC protocol 14–026 (Protocol PI: A. Plaas).

ORCID

Deva D. Chan https://orcid.org/0000-0003-1508-1045
Maleeha Mashiatulla https://orcid.org/0000-0003-2847-2766
Jun Li https://orcid.org/0000-0002-3257-9315
Ryan D. Ross https://orcid.org/0000-0003-3760-234X
Meghana Pendyala https://orcid.org/0000-0003-2968-1746
Amit Patwa https://orcid.org/0000-0002-9323-3262
Mark W. Grinstaff https://orcid.org/0000-0002-5453-3668
Anna Plaas https://orcid.org/0000-0001-5205-0892

REFERENCES

Adebayo, O. O., Ko, F. C., Wan, P. T., Goldring, S. R., Goldring, M. B., Wright, T. M., & van der Meulen, M. C. H. (2017). Role of subchondral bone properties and changes in development of load-induced osteoarthritis in mice. *Osteoarthritis and Cartilage*, *25*, 2108–2118.

Alliston, T., Hernandez, C. J., Findlay, D. M., Felson, D. T., & Kennedy, O. D. (2018). Bone marrow lesions in osteoarthritis: What lies beneath. *Journal of Orthopaedic Research*, *36*, 1818–1825.

Bailey, K. N., Nguyen, J., Yee, C. S., Dole, N. S., Dang, A., & Alliston, T. (2021). Mechanosensitive control of articular cartilage and subchondral bone homeostasis in mice requires osteocytic transforming growth factor beta signaling. *Arthritis & Rheumatology*, *73*, 414–425.

Bansal, P. N., Joshi, N. S., Entezari, V., Grinstaff, M. W., & Snyder, B. D. (2010). Contrast enhanced computed tomography can predict the glycosaminoglycan content and biomechanical properties of articular cartilage. *Osteoarthritis and Cartilage*, *18*, 184–191.

Bansal, P. N., Joshi, N. S., Entezari, V., Malone, B. C., Stewart, R. C., Snyder, B. D., & Grinstaff, M. W. (2011). Cationic contrast agents improve quantification of glycosaminoglycan (GAG) content by contrast enhanced CT imaging of cartilage. *Journal of Orthopaedic Research*, *29*, 704–709.

Bansal, P. N., Stewart, R. C., Entezari, V., Snyder, B. D., & Grinstaff, M. W. (2011). Contrast agent electrostatic attraction rather than repulsion to glycosaminoglycans affords a greater contrast uptake ratio and improved quantitative CT imaging in cartilage. *Osteoarthritis and Cartilage*, *19*, 970–976.

Bateman, J. F., Rowley, L., Belluoccio, D., Chan, B., Bell, K., Fosang, A. J., & Little, C. B. (2013). Transcriptomics of wild-type mice and mice lacking ADAMTS-5 activity identifies genes involved in osteoarthritis initiation and cartilage destruction. *Arthritis and Rheumatism*, *65*, 1547–1560.

Bhattarai, A., Makela, J. T. A., Pouran, B., Kroger, H., Weinans, H., Grinstaff, M. W., Toyras, J., & Turunen, M. J. (2021). Effects of human articular cartilage constituents on simultaneous diffusion of cationic and nonionic contrast agents. *Journal of Orthopaedic Research*, *39*, 771–779.

Bhattarai, A., Pouran, B., Makela, J. T. A., Shaikh, R., Honkanen, M. K. M., Prakash, M., Kroger, H., Grinstaff, M. W., Weinans, H., Jurvelin, J. S., & Toyras, J. (2020). Dual contrast in computed tomography allows earlier characterization of articular cartilage over single contrast. *Journal of Orthopaedic Research*, *38*, 2230–2238.

Boskey, A. L., DiCarlo, E., Paschalis, E., West, P., & Mendelsohn, R. (2005). Comparison of mineral quality and quantity in iliac crest biopsies from high- and low-turnover osteoporosis: An FT-IR microspectroscopic investigation. *Osteoporosis International*, *16*, 2031–2038.

Bouxsein, M. L., Boyd, S. K., Christiansen, B. A., Guldberg, R. E., Jepsen, K. J., & Muller, R. (2010). Guidelines for assessment of bone microstructure in rodents using micro-computed tomography. *Journal of Bone and Mineral Research*, *25*, 1468–1486.

Bouxsein, M. L., Myers, K. S., Shultz, K. L., Donahue, L. R., Rosen, C. J., & Beamer, W. G. (2005). Ovariectomy-induced bone loss varies among inbred strains of mice. *Journal of Bone and Mineral Research*, *20*, 1085–1092.

Burr, D. B., & Gallant, M. A. (2012). Bone remodelling in osteoarthritis. *Nature Reviews Rheumatology*, *8*, 665–673.

Calvo, E., Palacios, I., Delgado, E., Sanchez-Pernaute, O., Largo, R., Egido, J., & Herrero-Beaumont, G. (2004). Histopathological correlation of cartilage swelling detected by magnetic resonance imaging in early experimental osteoarthritis. *Osteoarthritis and Cartilage*, *12*, 878–886.

Chan, D. D., Li, J., Luo, W., Predescu, D. N., Cole, B. J., & Plaas, A. (2018). Pirfenidone reduces subchondral bone loss and fibrosis after murine knee cartilage injury. *Journal of Orthopaedic Research*, *36*, 365–376.

Chan, D. D., Xiao, W. F., Li, J., de la Motte, C. A., Sandy, J. D., & Plaas, A. (2015). Deficiency of hyaluronan synthase 1 (Has1) results in chronic joint inflammation and widespread intra-articular fibrosis in a murine model of knee joint cartilage damage. *Osteoarthritis and Cartilage*, *23*, 1879–1889.

Das Neves Borges, P., Forte, A. E., Vincent, T. L., Dini, D., & Marenzana, M. (2014). Rapid, automated imaging of mouse articular cartilage by microCT for early detection of osteoarthritis and finite element modelling of joint mechanics. *Osteoarthritis and Cartilage*, *22*, 1419–1428.

David, M. A., Smith, M. K., Pilachowski, R. N., White, A. T., Locke, R. C., & Price, C. (2017). Early, focal changes in cartilage cellularity and structure following surgically induced meniscal destabilization in the mouse. *Journal of Orthopaedic Research*, *35*, 537–547.

Deuerling, J. M., Rudy, D. J., Niebur, G. L., & Roeder, R. K. (2010). Improved accuracy of cortical bone mineralization measured by polychromatic microcomputed tomography using a novel high mineral density composite calibration phantom. *Medical Physics*, *37*, 5138–5145.

Doyran, B., Tong, W., Li, Q., Jia, H., Zhang, X., Chen, C., Enomoto-Iwamoto, M., Lu, X. L., Qin, L., & Han, L. (2017). Nanoindentation modulus of murine cartilage: A sensitive indicator of the initiation and progression of post-traumatic osteoarthritis. *Osteoarthritis and Cartilage*, *25*, 108–117.

Drevet, S., Favier, B., Lardy, B., Gavazzi, G., & Brun, E. (2022). New imaging tools for mouse models of osteoarthritis. *Geroscience*, *44*, 639–650.

Fang, H., Huang, L., Welch, I., Norley, C., Holdsworth, D. W., Beier, F., & Cai, D. (2018). Early changes of articular cartilage and subchondral bone in the DMM mouse model of osteoarthritis. *Scientific Reports*, *8*, 2855.

Ferguson, V. L., Ayers, R. A., Bateman, T. A., & Simske, S. J. (2003). Bone development and age-related bone loss in male C57BL/6J mice. *Bone*, *33*, 387–398.

Glasson, S. S., Blanchet, T. J., & Morris, E. A. (2007). The surgical destabilization of the medial meniscus (DMM) model of osteoarthritis in the 129/SvEv mouse. *Osteoarthritis and Cartilage*, *15*, 1061–1069.

Glasson, S. S., Chambers, M. G., Van Den Berg, W. B., & Little, C. B. (2010). The OARSI histopathology initiative—Recommendations for histological assessments of osteoarthritis in the mouse. *Osteoarthritis and Cartilage*, *18*(Suppl. 3), S17–S23.

Goldring, S. R. (2012). Alterations in periarticular bone and cross talk between subchondral bone and articular cartilage in osteoarthritis. *Therapeutic Advances in Musculoskeletal Disease*, *4*, 249–258.

Goldring, S. R., & Goldring, M. B. (2016). Changes in the osteochondral unit during osteoarthritis: Structure, function and cartilage-bone crosstalk. *Nature Reviews Rheumatology*, *12*, 632–644.

Hui Mingalone, C. K., Liu, Z., Hollander, J. M., Garvey, K. D., Gibson, A. L., Banks, R. E., Zhang, M., McAlindon, T. E., Nielsen, H. C., Georgakoudi, I., & Zeng, L. (2018). Bioluminescence and second harmonic generation imaging reveal dynamic changes in the inflammatory and collagen landscape in early osteoarthritis. *Laboratory Investigation*, *98*, 656–669.

Jia, H., Ma, X., Wei, Y., Tong, W., Tower, R. J., Chandra, A., Wang, L., Sun, Z., Yang, Z., Badar, F., Zhang, K., Tseng, W. J., Kramer, I., Kneissel, M., Xia, Y., Liu, X. S., Wang, J. H. C., Han, L., Enomoto-Iwamoto, M., & Qin, L. (2018). Loading-induced reduction in sclerostin as a mechanism of subchondral bone plate sclerosis in mouse knee joints during late-stage osteoarthritis. *Arthritis & Rheumatology*, *70*, 230–241.

Joshi, N. S., Bansal, P. N., Stewart, R. C., Snyder, B. D., & Grinstaff, M. W. (2009). Effect of contrast agent charge on visualization of articular cartilage using computed tomography: Exploiting electrostatic interactions for improved sensitivity. *Journal of the American Chemical Society*, *131*, 13234–13235.

Jung, Y. K., Han, M. S., Park, H. R., Lee, E. J., Jang, J. A., Kim, G. W., Lee, S. Y., Moon, D., & Han, S. (2018). Calcium–phosphate complex increased during subchondral bone remodeling affects earlystage osteoarthritis. *Scientific Reports*, *8*, 487.

Lakin, B. A., Grasso, D. J., Stewart, R. C., Freedman, J. D., Snyder, B. D., & Grinstaff, M. W. (2013). Contrast enhanced CT attenuation correlates with the GAG content of bovine meniscus. *Journal of Orthopaedic Research*, *31*, 1765–1771.

Lakin, B. A., Patel, H., Holland, C., Freedman, J. D., Shelofsky, J. S., Snyder, B. D., Stok, K. S., & Grinstaff, M. W. (2016). Contrast-enhanced CT using a cationic contrast agent enables non-destructive assessment of the biochemical and biomechanical properties of mouse tibial plateau cartilage. *Journal of Orthopaedic Research*, *34*, 1130–1138.

Li, J., Anemaet, W., Diaz, M. A., Buchanan, S., Tortorella, M., Malfait, A. M., Mikecz, K., Sandy, J. D., & Plaas, A. (2011). Knockout of ADAMTS5 does not eliminate cartilage aggrecanase activity but abrogates joint fibrosis and promotes cartilage aggrecan deposition in murine osteoarthritis models. *Journal of Orthopaedic Research*, *29*, 516–522.

Lim, N. H., Vincent, T. L., & Nissim, A. (2015). In vivo optical imaging of early osteoarthritis using an antibody specific to damaged arthritic cartilage. *Arthritis Research & Therapy*, *17*, 376.

Lim, N. H., Wen, C., & Vincent, T. L. (2020). Molecular and structural imaging in surgically induced murine osteoarthritis. *Osteoarthritis and Cartilage*, *28*, 874–884.

Lin, Y. Y., Tanaka, N., Ohkuma, S., Iwabuchi, Y., Tanne, Y., Kamiya, T., Kunimatsu, R., Huang, Y. C., Yoshioka, M., Mitsuyoshi, T., Tanimoto, K., Tanaka, E., & Tanne, K. (2010). Applying an excessive mechanical stress alters the effect of subchondral osteoblasts on chondrocytes in a co-culture system. *European Journal of Oral Sciences*, *118*, 151–158.

Lories, R. J., & Luyten, F. P. (2011). The bone-cartilage unit in osteoarthritis. *Nature Reviews Rheumatology*, *7*, 43–49.

Ma, H. L., Blanchet, T. J., Peluso, D., Hopkins, B., Morris, E. A., & Glasson, S. S. (2007). Osteoarthritis severity is sex dependent in a surgical mouse model. *Osteoarthritis and Cartilage*, *15*, 695–700.

Mashiatulla, M., Moran, M. M., Chan, D., Li, J., Freedman, J. D., Snyder, B. D., Grinstaff, M. W., Plaas, A., & Sumner, D. R. (2017). Murine articular cartilage morphology and compositional quantification with high resolution cationic contrast-enhanced muCT. *Journal of Orthopaedic Research*, *35*, 2740–2748.

Mashiatulla, M., Ross, R. D., & Sumner, D. R. (2017). Validation of cortical bone mineral density distribution using micro-computed tomography. *Bone*, *99*, 53–61.

Miyamoto, Y., Mabuchi, A., Shi, D., Kubo, T., Takatori, Y., Saito, S., Fujioka, M., Sudo, A., Uchida, A., Yamamoto, S., Ozaki, K., Takigawa, M., Tanaka, T., Nakamura, Y., Jiang, Q., & Ikegawa, S. (2007). A functional polymorphism in the 5′ UTR of GDF5 is associated with susceptibility to osteoarthritis. *Nature Genetics*, *39*, 529–533.

Muehleman, C., Green, J., Williams, J. M., Kuettner, K. E., Thonar, E. J., & Sumner, D. R. (2002). The effect of bone remodeling inhibition by zoledronic acid in an animal model of cartilage matrix damage. *Osteoarthritis and Cartilage*, *10*, 226–233.

Murphy, L., & Helmick, C. G. (2012). The impact of osteoarthritis in the United States: A population-health perspective: A population-based review of the fourth most common cause of hospitalization in U.S. adults. *Orthopaedic Nursing*, *31*, 85–91.

Nagira, K., Ikuta, Y., Shinohara, M., Sanada, Y., Omoto, T., Kanaya, H., Nakasa, T., Ishikawa, M., Adachi, N., Miyaki, S., & Lotz, M. (2020). Histological scoring system for subchondral

bone changes in murine models of joint aging and osteoarthritis. *Scientific Reports*, *10*, 10077.

Pan, J., Wang, B., Li, W., Zhou, X., Scherr, T., Yang, Y., Price, C., & Wang, L. (2012). Elevated cross-talk between subchondral bone and cartilage in osteoarthritic joints. *Bone*, *51*, 212–217.

Pritzker, K. P., Gay, S., Jimenez, S. A., Ostergaard, K., Pelletier, J. P., Revell, P. A., Salter, D., & van den Berg, W. B. (2006). Osteoarthritis cartilage histopathology: Grading and staging. *Osteoarthritis and Cartilage*, *14*, 13–29.

R Development Core Team. (2010). *R: A language and environment for statistical computing*. R Foundation for Statistical Computing.

Roschger, P., Paschalis, E. P., Fratzl, P., & Klaushofer, K. (2008). Bone mineralization density distribution in health and disease. *Bone*, *42*, 456–466.

RStudio Team. (2020). *RStudio: Integrated development for R*. RStudio, PBC.

Sanchez, C., Deberg, M. A., Piccardi, N., Msika, P., Reginster, J. Y., & Henrotin, Y. E. (2005). Osteoblasts from the sclerotic subchondral bone downregulate aggrecan but upregulate metalloproteinases expression by chondrocytes. This effect is mimicked by interleukin-6, -1beta and oncostatin M pretreated non-sclerotic osteoblasts. *Osteoarthritis and Cartilage*, *13*, 979–987.

Somerville, J. M., Aspden, R. M., Armour, K. E., Armour, K. J., & Reid, D. M. (2004). Growth of C57BL/6 mice and the material and mechanical properties of cortical bone from the tibia. *Calcified Tissue International*, *74*, 469–475.

Stewart, R. C., Bansal, P. N., Entezari, V., Lusic, H., Nazarian, R. M., Snyder, B. D., & Grinstaff, M. W. (2013). Contrast-enhanced CT with a high-affinity cationic contrast agent for imaging ex vivo bovine, intact ex vivo rabbit, and in vivo rabbit cartilage. *Radiology*, *266*, 141–150.

Utomo, L., Fahy, N., Kops, N., van Tiel, S. T., Waarsing, J., Verhaar, J. A. N., Leenen, P. J. M., van Osch, G., & Bastiaansen-Jenniskens, Y. M. (2021). Macrophage phenotypes and monocyte subsets after destabilization of the medial meniscus in mice. *Journal of Orthopaedic Research*, *39*, 2270–2280.

Valdes, A. M., & Spector, T. D. (2008). The contribution of genes to osteoarthritis. *Rheumatic Diseases Clinics of North America*, *34*, 581–603.

Vincent, T. L. (2020). Of mice and men: Converging on a common molecular understanding of osteoarthritis. *Lancet Rheumatology*, *2*, e633–e645.

Westacott, C. I., Webb, G. R., Warnock, M. G., Sims, J. V., & Elson, C. J. (1997). Alteration of cartilage metabolism by cells from osteoarthritic bone. *Arthritis and Rheumatism*, *40*, 1282–1291.

Wickham, H. (2016). *ggplot2: Elegrant graphics for data analysis*. Springer-Verlag.

Ziemian, S. N., Witkowski, A. M., Wright, T. M., Otero, M., & van der Meulen, M. C. H. (2021). Early inhibition of subchondral bone remodeling slows load-induced posttraumatic osteoarthritis development in mice. *Journal of Bone and Mineral Research*, *36*, 2027–2038.

SUPPORTING INFORMATION

Additional supporting information can be found online in the Supporting Information section at the end of this article.

How to cite this article: Chan, D. D., Mashiatulla, M., Li, J., Ross, R. D., Pendyala, M., Patwa, A., Grinstaff, M. W., Plaas, A., & Sumner, D. R. (2023). Contrast-enhanced micro-computed tomography of compartment and time-dependent changes in femoral cartilage and subchondral plate in a murine model of osteoarthritis. *The Anatomical Record*, *306*(1), 92–109. https://doi.org/10.1002/ar.25027